# RESIDENT SPACE OBJECT SHAPE AND MATERIAL ESTIMATION USING POLARIMETRIC DATA

## Andrew T. Swenson,[*] Christopher K. Nebelecky,[†] Daniel Wilkinson,[‡] and John L. Crassidis[§]

The utility of polarized light curves to ascertain space object material and shape properties is demonstrated. Passively collected light curves are a fundamental byproduct of electro-optical sensing and are abundantly available. Previous work has demonstrated that considering of the polarization of these light curves yields observable information regarding the material properties of the observed object. This paper expands that approach to incorporate shape properties of the space object. The approach uses a model-driven approached based on multiple-model adaptive estimation as the underlying framework. A simulation-based validation of the approach indicate that both shape and material properties are recoverable.

## INTRODUCTION

A key area to improved space domain awareness (SDA) is being able to characterize attributes of space objects (SOs) beyond just an object's orbit and ballistic coefficient. Of specific interest are the object's shape, attitude, surface properties, including surface materials, spin state, etc. All of these attributes can influence an object's orbit through the manifestation of non-conservative effects such as drag and solar radiation pressure. Further, these attributes can be insightful when assessing the structure, composition and capabilities of an SO. For large objects in low-Earth orbit, methods such as resolved imaging or radar cross-sectioning can be used to provide information about an object's shape or attitude. However, objects in higher orbits, such as geosynchronous orbit (GEO), are too distant for these methods to be effective using ground-based sensors.

Light curve data are the time-varying sensor wavelength-dependent apparent magnitude of energy (i.e. photons) scattered (reflected) off of an object along the line-of-sight to an observer. There are several aspects of using light curve data (temporal photometry) that make it particularly advantageous for object detection, identification and tracking. Because the apparent magnitude of the SO is a function of its size, orientation, and surface material properties, one or more of these characteristics should be recoverable from the photometric data. This can aid in the detection and identification of an SO after a catalog of spacecraft data with material properties, shape, and other attributes is developed. This may also prove to be powerful for never-seen-before objects or distant objects such as those in GEO and beyond.

---

[*]Graduate Student, Department of Mechanical & Aerospace Engineering, University at Buffalo, State University of New York, Amherst, New York, 14260-4400. Email: atswenso@buffalo.edu.

[†]Research Scientist, Department of Mechanical & Aerospace Engineering, University at Buffalo, State University of New York, Amherst, New York, 14260-4400. Email: ckn@buffalo.edu. Member AAS

[‡]Graduate Student, Department of Mechanical & Aerospace Engineering, University at Buffalo, State University of New York, Amherst, New York, 14260-4400. Email: dpwilkin@buffalo.edu.

[§]SUNY Distinguished Professor and Moog Endowed Chaired Professor of Innovation, Department of Mechanical & Aerospace Engineering, University at Buffalo, State University of New York, Amherst, New York, 14260-4400. Email: johnc@buffalo.edu. Fellow AAS.

Reference [1] first demonstrated the benefit of light curves to enhance SDA by its ability to enable attitude estimation of the SO. That work assumed that all attributes, such as shape and material properties, are well known. Their approach was extended to include combined orbit, attitude and surface parameters by combining astrometric (angles) and photometric (light curve) data.[2] However, significant difficulties must be overcome before light curve information can be utilized effectively. In particular, the measurement model is characterized by a high degree of non-linearity and there exists the distinct possibility for information dilution without sufficient observations. Multiple-model approaches were introduced to alleviate some of the difficulties. Reference [3] developed an approach to simultaneously estimate the orbit, attitude and shape of an unknown object from photometric data and has since been extended to include other SO characteristics such as mass[4] and spin state.[5] Being rooted in filtering techniques, these approaches are limited in practice by the initial conditions, specifically on the attitude, of the unknown object. This difficulty is being addressed in Ref. [6], which develops methods to identify initial static attitude estimates to initialize the attitude filter without any knowledge of the initial attitude configuration.

Further SO characterization is possible when once considers multispectral decomposition of the reflected light. Specifically, whereas monochromatic light curves can only render information about the SO's shape and attitude, multispectral imaging can be used to estimate the surface parameters of the SO. Hall et al. first demonstrated methods to estimate surface materials and their abundances from multispectral light curves. These methods estimate the fraction of each material that compose each facet of the SO, but assume that the attitude is perfectly known. Reference [7] utilizes a least-squares approach to determine the material composition in order to classify an unknown SO's bus type. While these methods consider the material makeup of the SO, they neglect the effect on the objects shape or dynamics. Since an SO's surface reflectance depends on the material makeup, and reflectance is a contributing factor in solar radiation pressure modeling, knowledge of the surface materials can ultimately yield more accurate dynamic modeling, especially for GEO objects.

Multispectral light curves are one method that has shown promise for determining SO material properties. Another method to ascertain SO material properties is through the use of polarized light curves. Incoming light reflecting off a surface will undergo a degree of polarization. The degree depends on the index of refraction and extinction coefficient, which are properties of the surface materials. Reference [8] demonstrates the benefit of polarized data by successfully identifying an unknown SO's material makeup using monochromatic polarized light. However, that work requires that the shape of the SO be known. The current work expands on that work to simultaneously estimate both the shape and material properties of an SO. Various studies will be shown that assess the observability of estimating both quantities. For example, it may be possible that multiple shape/material combinations produce the same estimate output. Still, this is the first attempt to estimate both quantities, which may lead to a realistic approach for the overall characterization of an SO.

The proposed approach leverages a data-driven, multiple-model adaptive estimation framework to identify, in real time, the hypothesized system model that best represents the observed data. The proposed approach is validated through three simulation use cases. The remainder of this paper is as follows. First, the observation model for light reflecting off a faceted SO is reviewed. Next, the model for polarized light reflections is introduced, including the Stokes vector which is the primary observation set used. The multiple-model adaptive estimator is then discussed followed by the simulation use cases.
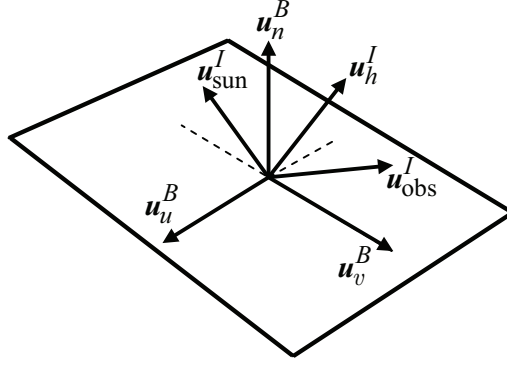
**Figure 1   Facet Reflection Geometry**

## LIGHT CURVE REFLECTANCE MODEL

This section provides and overview of the observation model considered in this work. The principal observations used are two components of the Stokes vector, a representation of polarized light. The observed light is assumed to be composed of light reflected off an object model comprised of a $N$ faceted sides.

### Faceted Shape Model

Space object (SO) models considered in this work consist of a finite number a flat facets that are assumed rigid. Curved surfaces can be modeled as a number of connected flat facets, with accuracy increasing with the number of facets. Each facet is described using a set of three orthonormal basis vectors ($\boldsymbol{u}_n^B$, $\boldsymbol{u}_u^B$, and $\boldsymbol{u}_v^B$) and the facet area $\mathcal{A}$, as shown in Figure 1. The vector $\boldsymbol{u}_n^B$ points in the direction of the outward normal to the facet while the vectors $\boldsymbol{u}_u^B$ and $\boldsymbol{u}_v^B$ span the plane of the facet. The notation $(\cdot)^B$ denotes that the vector is expressed in body coordinates. In this analysis, the object is assumed to be a rigid body so that the unit vectors $\boldsymbol{u}_n^B$, $\boldsymbol{u}_u^B$ and $\boldsymbol{u}_v^B$ do not change since they are expressed in the body frame.

The unit vector $\boldsymbol{u}_{\text{sun}}^I$ points from the SO to the Sun and the unit vector $\boldsymbol{u}_{\text{obs}}^I$ points from the SO to the observer and is expressed in inertial (superscript $I$) coordinates:

$$\boldsymbol{u}_{\text{sun}}^I = \frac{\boldsymbol{r}^I - \boldsymbol{r}_{\text{sun}}^I}{\|\boldsymbol{r}^I - \boldsymbol{r}_{\text{sun}}^I\|} \tag{1a}$$

$$\boldsymbol{u}_{\text{obs}}^I = \frac{\boldsymbol{r}^I - \boldsymbol{r}_{\text{obs}}^I}{\|\boldsymbol{r}^I - \boldsymbol{r}_{\text{obs}}^I\|} \tag{1b}$$

where $\boldsymbol{r}^I$ is the position vector of the SO, $\boldsymbol{r}_{\text{sun}}^I$ is the position of the sun and $\boldsymbol{r}_{\text{obs}}^I$ is the position vector of the observer, all referenced in an Earth-centered inertial coordinate system such as J2000.[9] The vector $\boldsymbol{u}_h^I$, known as the Sun-observer bisector, is the normalized half vector between $\boldsymbol{u}_{\text{sun}}^I$ and $\boldsymbol{u}_{\text{obs}}^I$:

$$\boldsymbol{u}_h^I = \frac{\boldsymbol{u}_{\text{sun}}^I + \boldsymbol{u}_{\text{obs}}^I}{\|\boldsymbol{u}_{\text{sun}}^I + \boldsymbol{u}_{\text{obs}}^I\|} \tag{2}$$

Note that $\boldsymbol{u}_{\text{sun}}^I$ and $\boldsymbol{u}_{\text{obs}}^I$ are time-varying due to the dependence on the satellite, Sun and observer positions at the specific time of observation.

A faceted object representation can be used to model the apparent magnitude of an observed object. The apparent magnitude is a measure of the brightness of the object, and is one of the typically reported quantities from electro-optical (EO) sensors. For an object consisting of $N$ facets, the apparent magnitude, $m_{\text{app}}$, can be represented by

$$m_{\text{app}} = -26.7 - 2.5 \log_{10} \left| \sum_{i=1}^{N} \frac{F_{\text{obs},i}}{C_{\text{sun,vis}}} \right| \tag{3}$$

where $-26.7$ is the apparent magnitude of the Sun, and $C_{\text{sun,vis}} = 455$ W/m$^2$ is the power per square meter of visible sunlight impinging on the SO. The fraction of light that is reflected towards the observer from facet $i$, $F_{\text{obs},i}$, is given by

$$F_{\text{obs},i} = \frac{F_{\text{sun},i} \, \mathcal{A}_i \, (\boldsymbol{u}_{n,i}^I \cdot \boldsymbol{u}_{\text{obs}}^I)}{d^2} \tag{4}$$

where $d$ is the distance between the observer and the SO, and $\mathcal{A}_i$ is the area of the $i^{\text{th}}$ facet. The fraction of visible sunlight that strikes an object (and is not absorbed) is

$$F_{\text{sun},i} = C_{\text{sun,vis}} \, \rho_{\text{total},i} \, (\boldsymbol{u}_{n,i}^I \cdot \boldsymbol{u}_{\text{sun}}^I) \tag{5}$$

Note that in Eq. (3), the summation only incorporates facets that are actively reflecting light towards the observer. If either the angle between the surface normal and the observer's direction or the angle between the surface normal and the Sun direction is greater than $\pi/2$ then there is no light reflected toward the observer. If this is the case then the fraction of visible light is set to $F_{\text{sun},i} = 0$. The final term, $\rho_{\text{total},i}$ the total bidirectional reflectance distribution function (BRDF), which is described in the next section.

**Unpolarized BRDF Model**

A BRDF is a mathematical modeling of how light reflects off an opaque surface. BRDFs are functions of two input variables, the directions of the incoming and outgoing light. The total BRDF output, $\rho_{\text{total},i}$, is comprised of a specular component ($\rho_{\text{spec},i}$) and a diffuse component ($\rho_{\text{diff},i}$):

$$\rho_{\text{total},i} = \rho_{\text{spec},i} + \rho_{\text{diff},i} \tag{6}$$

The diffuse component represents light that is scattered equally in all directions (Lambertian), and the specular component represents light that is concentrated about some direction (mirror-like). The BRDF model used in this work is a modified version of the Phong model described in Ref. [10] which is summarized here. The specular term of the BRDF is given by

$$\rho_{\text{spec},i} = \frac{\sqrt{(\eta_{u,i}+1)(\eta_{v,i}+1)}}{8\pi} \frac{(\boldsymbol{u}_{n,i}^I \cdot \boldsymbol{u}_h^I)}{\boldsymbol{u}_{n,i}^I \cdot \boldsymbol{u}_{\text{sun}}^I + \boldsymbol{u}_{n,i}^I \cdot \boldsymbol{u}_{\text{obs}}^I - (\boldsymbol{u}_{n,i}^I \cdot \boldsymbol{u}_{\text{sun}}^I)(\boldsymbol{u}_{n,i}^I \cdot \boldsymbol{u}_{\text{obs}}^I)} \left\{ \frac{\eta_{u,i}(\boldsymbol{u}_h^I \cdot \boldsymbol{u}_{u,i}^I)^2 + \eta_{v,i}(\boldsymbol{u}_h^I \cdot \boldsymbol{u}_{v,i}^I)^2}{\left(1 - \left[\boldsymbol{u}_{n,i}^I \cdot \boldsymbol{u}_h^I\right]^2\right)} \right\} F_{\text{reflect},i} \tag{7}$$

where $F_{\text{reflect},i}$ is the Fresnel reflectance:

$$F_{\text{reflect},i} = R_{\text{spec},i} + (1 - R_{\text{spec},i})(1 - \boldsymbol{u}_{\text{sun}}^I \cdot \boldsymbol{u}_{h,i}^I)^5 \tag{8}$$

If the surface was perfectly smooth, all of the Fresnel reflectance would be directed along the reflectance direction, expressed in body coordinates as

$$\boldsymbol{u}_{\text{reflect}}^{B} = \boldsymbol{u}_{\text{sun}}^{B} - 2(\boldsymbol{u}_{\text{sun}}^{B} \cdot \boldsymbol{u}_{n}^{B})\boldsymbol{u}_{n}^{B} \tag{9}$$

where $\boldsymbol{u}_{\text{sun}}^{B}$ is the Sun vector in body coordinates. However, real materials have some level of surface roughness, which results in many small surface normals that are oriented in different directions. Therefore, the specular reflectance can be thought of as a cone distributed around the specular reflection direction given in Eq. (9), with the distribution (in the local $u$ and $v$ directions) defined by the terms $\eta_u$ and $\eta_v$. Throughout this work, $n_{u,i} = n_{v,i}$ is assumed.

The diffuse term of the BRDF is given by

$$\rho_{\text{diff},i} = \left(\frac{28R_{\text{diff},i}}{23\pi}\right)(1 - R_{\text{spec},i})\left[1 - \left(1 - \frac{\boldsymbol{u}_{n,i}^{I} \cdot \boldsymbol{u}_{\text{sun}}^{I}}{2}\right)^5\right]\left[1 - \left(1 - \frac{\boldsymbol{u}_{n,i}^{I} \cdot \boldsymbol{u}_{\text{obs}}^{I}}{2}\right)^5\right] \tag{10}$$

In Eqs. (7) and (10) the terms $R_{\text{spec},i}$ and $R_{\text{diff},i}$ are the specular and diffuse reflectance coefficients of the $i^{\text{th}}$ facet. This work assumes surfaces are opaque (non-transmitting) and non-absorbing so that $R_{\text{spec},i} + R_{\text{diff},i} = 1$.

**Polarized Light**

While the scalar $m_{\text{app}}$ gives the total intensity of the reflected light, it does not contain information about the light's polarization. However, the Fresnel reflectance of unpolarized light (such as sunlight) will be polarized so long as the vectors $\boldsymbol{u}_{h}^{I}$ and $\boldsymbol{u}_{n}^{I}$ are not aligned. One common example of this phenomenon can be observed by looking at the surface of a body of water or a metal roof while wearing polarized sunglasses. Since many surfaces of SOs are relatively flat, they will produce polarized Fresnel reflectance components. It is this phenomenon that this work seeks to exploit.

The most common representation for polarized light is through the Stokes vector. The Stokes vector, $\boldsymbol{S}$, is a four dimensional vector defined as:

$$\boldsymbol{S} = \begin{bmatrix} S_0 & S_1 & S_2 & S_3 \end{bmatrix}^T \tag{11}$$

where $S_0$ describes the total energy in a light beam and is conceptually equivalent to $m_{\text{app}}$ in Eq. (3), $S_1$ describes the amount of linear horizontal or vertical polarization, $S_2$ describes the amount of $\pm 45°$ linear polarization, and $S_3$ describes the amount of right- or left-handed circular polarization.[11] An alternative representation of the Stokes vector normalizes the components by $S_0$:

$$\hat{\boldsymbol{S}} \equiv \begin{bmatrix} 1 \\ S_1/S_0 \\ S_2/S_0 \\ S_3/S_0 \end{bmatrix} \tag{12}$$

This representation permits the polarization state of the light beam without containing its total intensity and is useful for describing a number of important polarization states. Randomly polarized (or "unpolarized") light has $\hat{\boldsymbol{S}} = \begin{bmatrix} 1 & 0 & 0 & 0 \end{bmatrix}^T$. Linear horizontal polarization has $\hat{\boldsymbol{S}} = \begin{bmatrix} 1 & 1 & 0 & 0 \end{bmatrix}^T$, and linear vertical polarization has $\hat{\boldsymbol{S}} = \begin{bmatrix} 1 & -1 & 0 & 0 \end{bmatrix}^T$. Linear $+45°$ polarization has $\hat{\boldsymbol{S}} = \begin{bmatrix} 1 & 0 & 1 & 0 \end{bmatrix}^T$,

and linear $-45°$ polarization has $\hat{\boldsymbol{S}} = \begin{bmatrix} 1 & 0 & -1 & 0 \end{bmatrix}^T$. Right-handed circular polarization has $\hat{\boldsymbol{S}} = \begin{bmatrix} 1 & 0 & 0 & 1 \end{bmatrix}^T$, and left-handed circular polarization has $\hat{\boldsymbol{S}} = \begin{bmatrix} 1 & 0 & 0 & -1 \end{bmatrix}^T$.

As mentioned, incident light beams reflecting off a surface become polarized. This transformation can be represented through the Mueller matrix, $M$, which transforms the Stokes vector of an incoming light beam, $\boldsymbol{S}_{\mathrm{in}}$, to that of the transmitted or reflected light beam, $\boldsymbol{S}_{\mathrm{out}}$:

$$\hat{\boldsymbol{S}}_{\mathrm{out}} = M\hat{\boldsymbol{S}}_{\mathrm{in}} \tag{13}$$

The Mueller matrix for polarimetric Fresnel reflection, $M_F$, is given by[11]

$$M_F = \frac{1}{2} \begin{bmatrix} R_s + R_p & R_s - R_p & 0 & 0 \\ R_s - R_p & R_s + R_p & 0 & 0 \\ 0 & 0 & 2\mathrm{Re}(r_s r_p^*) & 2\mathrm{Im}(r_s r_p^*) \\ 0 & 0 & -2\mathrm{Im}(r_s r_p^*) & 2\mathrm{Re}(r_s r_p^*) \end{bmatrix} \tag{14}$$

where $r_s = \sqrt{R_s}$, $r_p = \sqrt{R_p}$, $\mathrm{Re}(\cdot)$ and $\mathrm{Im}(\cdot)$ refer to the real imaginary parts, respectively, and the superscript $*$ denotes the complex conjugate. Also, $R_s$ is the Fresnel reflectance coefficient for radiation perpendicular to the plane of incident flux, and $R_p$ is the Fresnel reflectance coefficient for radiation parallel to the plane of incident flux.

Since sunlight is randomly polarized, it has a Stokes vector of $\hat{\boldsymbol{S}}_{\mathrm{in}} = \begin{bmatrix} 1 & 0 & 0 & 0 \end{bmatrix}^T$. Thus, the Stokes vector of the Fresnel reflection is

$$\hat{\boldsymbol{S}}_F = \begin{bmatrix} R_s + R_p \\ R_s - R_p \\ 0 \\ 0 \end{bmatrix} \tag{15}$$

From this, it is seen that Fresnel reflectance of randomly polarized light has linear horizontal or vertical polarization, but no $\pm 45°$ or circular polarization. Thus, in the case of reflected sunlight, only the $S_0$ and $S_1$ terms are non-zero and can be leveraged.

**Polarized BRDF Model**

The BRDF model presented in the earlier section is now extended to the polarized case. The polarized $s$- and $p$-components of the Fresnel reflection must be computed. The terms $R_s$ and $R_p$ can be computed as[11]

$$R_s = \left| \frac{(n^2 - \sin^2\theta_i)^{1/2} - \cos\theta}{(n^2 - \sin^2\theta)^{1/2} + \cos\theta} \right|^2 \tag{16a}$$

$$R_p = \left| \frac{n^2\cos\theta_i - (n^2 - \sin^2\theta_i)^{1/2}}{n^2\cos\theta_i + (n^2 - \sin^2\theta_i)^{1/2}} \right|^2 \tag{16b}$$

where $n \equiv n_2/n_1$ is the relative index of refraction of the reflected medium to the medium of the incident beam and $\theta$ is the angle of incidence. For a model consisting of flat facets the angle of incidence is the angle between the $\boldsymbol{u}_{\mathrm{sun}}^I$ and $\boldsymbol{u}_{\mathrm{obs}}^I$ from Eq. (1):

$$\theta = \cos^{-1}\left( \boldsymbol{u}_{\mathrm{sun}}^I \cdot \boldsymbol{u}_{\mathrm{obs}}^I \right) \tag{17}$$

For reflecting objects in a vacuum (such as space), $n_1 = 1$, yielding $n = n_2$.

Equation (16) can be expanded to[12]

$$R_s = \frac{a^2 + b^2 - 2\,a\cos\theta + \cos^2\theta}{a^2 + b^2 + 2\,a\cos\theta + \cos^2\theta} \tag{18a}$$

$$R_p = R_s \frac{a^2 + b^2 - 2\,a\sin\theta\tan\theta + \sin^2\theta\tan^2\theta}{a^2 + b^2 + 2\,a\sin\theta\tan\theta + \sin^2\theta\tan^2\theta} \tag{18b}$$

where

$$a^2 = \frac{1}{2}\left\{\sqrt{(m^2 - k^2 - \sin^2\theta)^2 + 4m^2k^2} + m^2 - k^2 - \sin^2\theta\right\} \tag{19a}$$

$$b^2 = \frac{1}{2}\left\{\sqrt{(m^2 - k^2 - \sin^2\theta)^2 + 4m^2k^2} - (m^2 - k^2 - \sin^2\theta)\right\} \tag{19b}$$

where the complex representation for the index of refraction, $n = m + ik$ is used; $m$ is the real part of the refractive index and $k$ is the extinction coefficient.[13] For dielectric materials, $k = 0$ and thus $n$ is real, whereas $k$ is nonzero for conductors (such as metals) resulting in a complex $n$.

The terms $R_s$ and $R_p$ are the components of the Fresnel reflection in the planes perpendicular and parallel to the plane of the incident flux, respectively. These components are carried forward in place of $F_{\text{reflect},i}$ in Eq. (7). That is:

$$\rho_{\text{spec},s,i} = \frac{\sqrt{(\eta_{u,i}+1)(\eta_{v,i}+1)}}{8\pi}\frac{\left(\boldsymbol{u}_{n,i}^I \cdot \boldsymbol{u}_h^I\right)\left\{\dfrac{\eta_{u,i}(\boldsymbol{u}_h^I \cdot \boldsymbol{u}_{u,i}^I)^2 + \eta_{v,i}(\boldsymbol{u}_h^I \cdot \boldsymbol{u}_{v,i}^I)^2}{\left(1 - \left[\boldsymbol{u}_{n,i}^I \cdot \boldsymbol{u}_h^I\right]^2\right)}\right\}}{\boldsymbol{u}_{n,i}^I \cdot \boldsymbol{u}_{\text{sun}}^I + \boldsymbol{u}_{n,i}^I \cdot \boldsymbol{u}_{\text{obs}}^I - (\boldsymbol{u}_{n,i}^I \cdot \boldsymbol{u}_{\text{sun}}^I)(\boldsymbol{u}_{n,i}^I \cdot \boldsymbol{u}_{\text{obs}}^I)}R_{s,i} \tag{20}$$

with an analogous result for $\rho_{\text{spec},p,i}$. The diffuse coefficients in the $s$- and $p$- directions are given by

$$\rho_{\text{diff},x,i} = \frac{T_x}{T_s + T_p}\rho_{\text{diff},i} \qquad x = \{s, p\} \tag{21}$$

where $T_s = 1 - R_s$ and $T_p = 1 - R_p$ and $\rho_{\text{diff},i}$ is given by Eq. (10). The total BRDF in the $s$- and $p$- directions is then computed as

$$\rho_{\text{total},i,x} = \rho_{\text{spec},i,x} + \rho_{\text{diff},i,x} \qquad x = \{s, p\} \tag{22}$$

These terms are then used in Eq. (5) and (4), ultimately yielding $F_{\text{obs},i,s}$ and $F_{\text{obs},i,p}$ reflecting facets. These values are summed over all reflecting facets:

$$F_{\text{obs},x} = \sum_{i=1}^{N} F_{\text{obs},i,x} \qquad x = \{s, p\} \tag{23}$$

The non-zero components of the Stokes vector can then be computed as

$$\begin{bmatrix}\hat{S}_0\\ \hat{S}_1\end{bmatrix} = \begin{bmatrix}F_{\text{obs},s} + F_{\text{obs},p}\\ F_{\text{obs},s} - F_{\text{obs},p}\end{bmatrix} \tag{24}$$

Note again that $\hat{S}_0$ is equivalent to the apparent magnitude, with the mapping between the two given by

$$m_{\text{app}} = -26.7 - 2.5\log_{10}\left(\frac{\hat{S}_0}{C_{\text{sun,vis}}}\right) \tag{25}$$

**Shape and Material Estimation using Multiple-Model Adaptive Estimation**

This work focuses on leveraging the Stokes vector to aid in the identification of SO shape and material properties. Neither the material properties $m$ or $k$, nor the shape are directly observable using traditional real time estimation approaches. To overcome the observability issue, a multiple-model adaptive estimation (MMAE) approach is used to identify the shape and material characteristics of the observed object.

MMAE is a recursive algorithm that uses a bank of estimators, each dependent on a particular hypothesis, $\boldsymbol{p}^{(\ell)}$, to determine an estimate based upon an unknown physical process under consideration. Hypotheses in this context correspond to different mathematical models, or parameter values that underpin the observed system. Each model is weighted according to the likelihood function, i.e. the likelihood that a particular hypothesis resulted in the observed measurement, and are updated in a recursive manner to capture the temporal performance of a particular hypothesis:

$$
\begin{aligned}
\varpi_k^{(\ell)} &= \varpi_{k-1}^{(\ell)} p\left(\tilde{\boldsymbol{y}}_{k-1} | \hat{\boldsymbol{x}}_{k-1}^{-(\ell)}\right) \\
\varpi_k^{(\ell)} &\leftarrow \frac{\varpi_k^{(\ell)}}{\displaystyle\sum_{j=1}^{M} \varpi_k^{(j)}}
\end{aligned}
\tag{26}
$$

where the weight $\varpi_k^{(\ell)} \equiv p\left(\boldsymbol{p}^{(\ell)} | \tilde{\boldsymbol{Y}}_k\right)$ is the probability that hypothesis $\ell$ represents the system model conditioned on the observation set up to the current time $k$, $\tilde{\boldsymbol{Y}}_k = \{\tilde{\boldsymbol{y}}_1, \tilde{\boldsymbol{y}}_2, \ldots, \tilde{\boldsymbol{y}}_k\}$. The likelihood function can be computed based on the output from the individual estimator, $p\left(\tilde{\boldsymbol{y}}_k | \hat{\boldsymbol{x}}_k^{-(\ell)}\right)$. Assuming a Kalman filter or other sequential Gaussian estimator, the likelihood is given by

$$
p\left(\tilde{\boldsymbol{y}}_k | \hat{\boldsymbol{x}}_k^{-(\ell)}\right) = \frac{1}{\det\left(2\pi S_k^{(\ell)}\right)^{1/2}} \exp\left\{-\frac{1}{2} \boldsymbol{e}_k^{(\ell)T} S_k^{(\ell)-1} \boldsymbol{e}_k^{(\ell)}\right\}
\tag{27}
$$

where $\boldsymbol{e}_k^{(\ell)} \equiv \tilde{\boldsymbol{y}}_k - \hat{\boldsymbol{y}}_k^-$ is the measurement residual and $S_k^{(\ell)}$ is the innovations covariance from the estimator. For a more detailed description of the MMAE framework, including the fusion of state estimates from the bank of filters, readers are referred to Refs. [3] and [14].

## SIMULATION RESULTS

A set of simulation results are shown to demonstrate the capability of the developed approach. Three simulation cases are presented. Case 1 considers a situation where all of the shape models within the hypothesis set are the same and only the material differs between models and is meant to demonstrate the ability to identify material properties using the polarimetric data. In case 2, multiple shape models are used while the material is held constant, demonstrating the ability to discern shape using the proposed approach. The last case considers multiple shape and material combinations, consistent with a more rigorous real world use case of different satellites and/or debris objects.

For all simulations, an SO is in near-GEO orbit with orbital elements given by $a = 42,164$ km, $e = 0.01$, $i = 20°$, $\Omega = 279°$, $\omega = 208°$, and $M_0 = 160°$. The simulation epoch is 15 October 2013 at 06:18:15 GST. The SO's attitude quaternion is randomly generated, and the angular rate of the SO in body coordinates is $\boldsymbol{\omega}_{B/I}^B = [-2475.1 \ 1031.3 \ 1650.1]^T$ deg/hr. The state of the system

evolves according to

$$\ddot{\boldsymbol{r}} = -\frac{\mu}{r^3}\boldsymbol{r} \tag{28a}$$

$$\dot{\mathbf{q}} = \frac{1}{2}\Xi\left(\boldsymbol{q}\right)\boldsymbol{\omega}_{B/I}^B \tag{28b}$$

$$\dot{\boldsymbol{\omega}}_{B/I}^B = \mathbf{0} \tag{28c}$$

where $\boldsymbol{r}$ is the SO's position and $\mathbf{q}$ is the SO's attitude quaternion. Each of the estimators within the MMAE framework is executing an Unscented filter as the underlying state estimation technique.[3] All test cases assume that the position, velocity and angular rate states are perfectly known and that the initial attitude state is corrupted by $10°$ of attitude error in each body axis. Initial standard deviations in the states are $15°$ degrees in attitude, 24 deg/hr in angular rate, 10 km in position and 100 m/s in velocity.

Topocentric right ascension, declination, and the $S_0$ and $S_1$ Stokes parameters are generated using a ground station located at $149.0°$ W, $29.6°$ N and 1.631 km. Measurements are constructed using instantaneous geometry. Astrometric observations are corrupted by zero-mean Gaussian white noise with standard deviations of 3 arc-seconds. Measurement noise on the Stokes parameters is also zero-mean, Gaussian white noise with standard deviations of

$$\sigma_{S_0} = \sigma_{S_1} = \frac{4\sqrt{2}\,h\,c}{\lambda\pi D^2 Q\Delta t}\sigma_{n_e} \tag{29}$$

where $\sigma_{n_e}$ is the spectral density of noise in the electron count given by:

$$\sigma_{n_e} = \sqrt{\sigma_d^2\Delta t^2 + \sigma_r^2} \tag{30}$$

In Eqs. (29) and (30), $h$ is Planck's constant, $c$ is the speed of light in a vacuum, $\lambda = 500$ nm is the wavelength of the photons, $\sigma_d = 1$ is the spectral density of dark current, $\sigma_r = 6$ is the spectral density of the read noise, $\Delta t = 1\,\mathrm{s}$ is the exposure time of the image, $D = 2.4\,\mathrm{m}$ is the aperture diameter, and $Q = 0.62$ is the quantum efficiency. For more details on the noise model and parameters for the polarimeter see Ref. [15]. Observations are simulated for 30 minutes at 1 Hz. When generating photometric observations, it is assumed that the Sun is the sole source of illumination.

### Table 1  Shape Model Dimensions

| Dimension | Small Box | Plate | Large Box |
|---|---|---|---|
| Height (m) | 1.3 | 1.8 | 2.0 |
| Width (m) | 1.4 | 1.75 | 2.1 |
| Depth (m) | 1.2 | 0.175 | 2.2 |

### Table 2  Material Model Properties

| Material | $m$ | $k$ | $\eta_u,\ \eta_v$ | $R_{\mathrm{diff}}$ |
|---|---|---|---|---|
| Gallium Arsenide | 3.8570 | 0.1980 | 1000 | 0.02 |
| Aluminum | 1.1987 | 7.0488 | 100 | 0.0 |
| Gold | 0.2773 | 2.9278 | 100 | 0.0 |
| Kapton | 1.4950 | 9.2e-5 | 515 | 0.3 |

The models, shape and material, used for the use cases are shown in Tables 1 and 2, and in Fig. 2. For all cases, SO models are assumed to be constructed of a single material, e.g. aluminum or another material. Case 1 considers that all models within the bank have the same shape. The bank, consisting of four models, is populated with small boxes, with differing materials. This case is conceptually the same as those of Ref. [8], and serves to validate the proposed implementation. The true material for this case is Kapton, which is quickly identified as shown in the model weights presented in Figure 3(a).



(a) Small Box          (b) Thin Plate          (c) Large Box
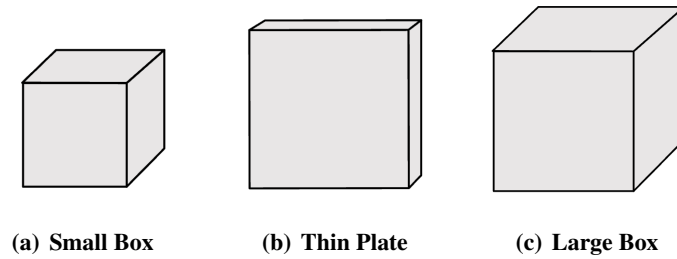
**Figure 2   Shape Models**

The second case considers differing shape models, but all constructed of the same material, in this case aluminum. The true system model is a small box. Model weights for this case can be found in Figure 2(a). Initially, the two box shapes share an equal weight before the small box shape is identified. Again, this is a relatively benign case, consistent with the simulation cases presented in Ref. [3], except that polarized light is used in lieu of monochromatic light.
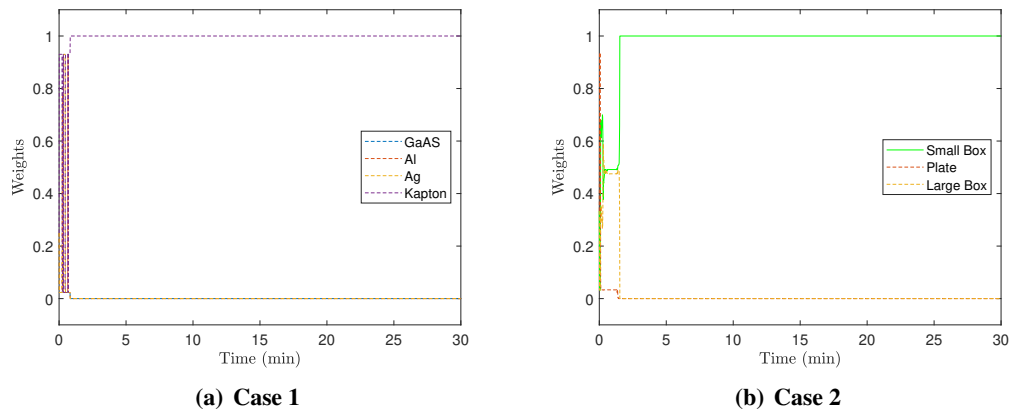


(a) Case 1                              (b) Case 2

**Figure 3   MMAE Model Weights for Cases 1 and 2**

The final use case considers a more realistic case where the model bank considers two different shape factors, each represented as being comprised of two different materials. The shapes considered are the plate and large box and the materials are gallium arsenide (GaAs) and aluminum. The truth model in this case is a GaA plate, similar to a broken off solar panel. The model weights for this case can be found in Figure 4(a). As can be seen, the correct model is immediately chosen

with a high probability. This is not unexpected given the drastic differences between the material properties of GaAs and aluminum. Specifically, GaAs creates both specular and diffuse reflections while aluminum will only create specular reflections, since pure metals do not exhibit the subsurface scattering behavior that is responsible for most specular reflection.[8] This result demonstrates the power in utilizing polarized light when considering material properties as one of the unknown system parameters. The state estimate errors for this case are also shown. Figure 4(b) displays the root-mean-squared error and corresponding $3\sigma$ covariance bounds from this case. All states converge nicely and are well contained within the covariance bounds, displaying consistency in the estimates.
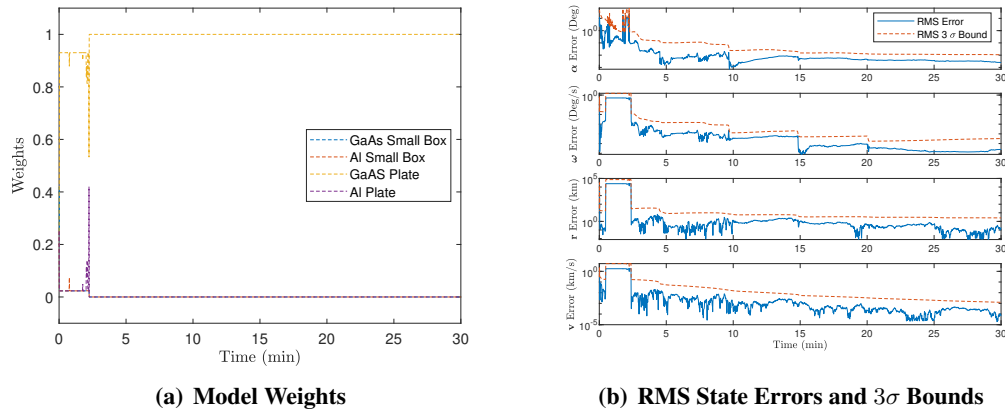


(a) Model Weights



(b) RMS State Errors and $3\sigma$ Bounds

**Figure 4   Case 3 Results**

## CONCLUSIONS

The ability to estimate material and shape properties of unknown space objects is presented. A multiple-model adaptive estimation framework is utilized to determine the most probable object shape and material composition. The Stokes vector representation of the polarized light is used as the enabling observations for this technique. Polarized light is used as the degree of polarization in reflected sunlight can be directly attributed to the material properties of the space object's surface materials. The presented approach has been demonstrated to produce accurate characterization results when both the material and shape of the object are unknown, but represented as part of a bank of candidate models. The developed approach provides one way to estimate material properties from unresolved imaging. Enhancements may be possible by augmenting the developed approach with multispectral imaging; a technique known to facilitate space object material characterization. Future work includes the fusion of these two techniques, as well as using polarized light curves to characterize more exquisite space object models comprised of multiple materials and complex shapes.

## ACKNOWLEDGEMENT

cal discussions and insight from Dr. Andrew D. Dianetti from the Air Force Research Laboratory (AFRL).

## REFERENCES

[1] C. J. Wetterer and M. Jah, "Attitude Estimation from Light Curves," *Journal of Guidance, Control and Dynamics*, Vol. 32, Sept.-Oct. 2009, pp. 1648–1651, doi:10.2514/1.62986.

[2] C. J. Wetterer, C. C. Chow, J. L. Crassidis, and R. Linares, "Simultaneous Position Velocity, Attitude, Angular Rates, and Surface Parameter Estimation Using Astrometric and Photometric Observations," *16th International Conference on Information Fusion*, Piscataway, NJ, IEEE, July 2013, pp. 997–1004. doi:10.2514/6.2013-5005.

[3] R. Linares, M. K. Jah, J. L. Crassidis, and C. K. Nebelecky, "Space Object Shape Characterization and Tracking Using Light Curve and Angles Data," *Journal of Guidance, Control, and Dynamics*, Vol. 37, No. 1, 2014, p. 13–25, doi:10.2514/1.62986.

[4] R. Linares, M. K. Jah, and J. L. Crassidis, "Space Object Area-to-Mass Estimation Using Multiple Model Approaches," *35th AAS Guidance and Control Conference*, Feb. 2012.

[5] R. Linares and J. L. Crassidis, "Space Object Classification Using Data Driven and Model Driven Methods," *26th AAS/AIAA Spaceflight Mechanics Meeting*, Feb. 2016.

[6] S. R. Gagnon and J. L. Crassidis, "Augmenting Light Curve Based Attitude Estimation with Geometric Information," *AIAA SciTech Forum*, San Diego, CA, Jan. 2023. AIAA 2022-1767, doi:10.2514/6.2022-1767.

[7] K. J. Abercromby, J. Rapp, D. Bedard, P. Seitzer, T. Cardona, H. Cowardin, E. Barker, and S. Lederer, "Comparisons of Constrained Least Squares Model Versus Human-in-the-Loop for Spectral Unmixing to Determine Material Type of GEO Debris," *6th European Conference on Space Debris*, April 2013.

[8] A. D. Dianetti and J. L. Crassidis, "Resident Space Object Characterization Using Polarized Light Curves," *Journal of Guidance, Control and Dynamics*, Vol. 46, Feb. 2023, p. 246–263, doi:10.2514/1.G006847.

[9] D. A. Vallado, *Fundamentals of Astrodynamics and Applications*, pp. 574–578. New York, NY: McGraw-Hill, $3^{rd}$ ed., 2007.

[10] M. Ashikmin and P. Shirley, "An Anisotropic Phong Light Reflection Model," Tech. Rep. UUCS-00-014, University of Utah, Salt Lake City, UT, 2000.

[11] J. Schott, *Fundamentals of Polarimetric Remote Sensing*. Society of Photo-Optical Instrumentation Engineers, 2009.

[12] P. Shirley, *Physically Based Lighting Calculations for Computer Graphics*. PhD thesis, University of Illinois at Urbana-Champaign, 1991.

[13] J. Stryjewski, D. Hand, D. Tyler, S. Murali, M. Roggemann, and N. Peterson, "Real Time Polarization Light Curves for Space Debris and Satellites," *Advanced Maui Optical and Space Surveillance Technologies Conference*, Sept. 2010.

[14] C. K. Nebelecky, *New Variations of Multiple Model Adaptive Estimation for Improved Tracking and Identification*. PhD thesis, University at Buffalo, The State University of New York, 2014.

[15] A. D. Dianetti, *Resident Space Object Characterization Using Polarized and Multispectral Light Curves*. PhD thesis, University at Buffalo, The State University of New York, 2020.